

Atom probe tomographic study of a friction-stir-processed Al–Mg–Sc alloy

Nhon Q. Vo^{a,*}, David C. Dunand^a, David N. Seidman^{a,b}

^a Department of Materials Science and Engineering, Northwestern University, 2220 Campus Drive, Evanston, IL 60208-3108, USA

^b Northwestern University Center for Atom-Probe Tomography, Northwestern University, 2220 Campus Drive, Evanston, IL 60208-3108, USA

Received 12 June 2012; received in revised form 30 August 2012; accepted 5 September 2012

Available online 5 October 2012

Abstract

The microstructure of a twin-roll-cast Al–4.5Mg–0.28Sc at.% alloy after friction-stir processing, performed at two tool rotational rates, was investigated by atom probe tomography. Outside the stir zone, the peak-aged alloy contains a high number density ($\sim 8.0 \times 10^{23} \text{ m}^{-3}$) of $\sim 1.5 \text{ nm}$ radius Al_3Sc (L_{12}) precipitates with a minor Mg content, providing an increase of $\sim 600 \text{ MPa}$ in the Vickers microhardness. In the stir zone of the sample processed at 400 rpm rotational rate, the microhardness increase is mainly due to grain refinement, rather than precipitate strengthening, because the Al_3Sc precipitates, with spherical lobed cuboids and platelet-like morphology, grow and coarsen to a 10–20 nm radius. The Sc supersaturation across the stir-processed zone has a concentration gradient, which is higher on the retreating side and lower on the advancing side of the friction-stir tool. Hence, after aging at 290 °C for 22 h, the microhardness increase within the stir zone also displays a gradient due to precipitate strengthening with varying precipitate volume fractions. In the stir zone for the sample processed at 325 rpm rotational rate, the microhardness increase is also predominantly due to grain refinement, as coarse Al_3Sc precipitates form heterogeneously at grain boundaries with a platelet-like morphology. The hardness remains unchanged after a 290 °C aging treatment. This is because the Al_3Sc precipitates are highly heterogeneously distributed due to a combination of a small Sc supersaturation (0.05 at.%) in the matrix, the existence of dislocations, and a large area per unit volume of grain boundaries ($\sim 4\text{--}6 \times 10^6 \text{ m}^{-1}$).

© 2012 Acta Materialia Inc. Published by Elsevier Ltd. All rights reserved.

Keywords: Al–Mg–Sc alloy; Friction-stir process; Atom probe tomography; Strengthening

1. Introduction

Traditional high-performance aluminum alloys, such as the 2xxx and 7xxx series, have a maximum operating temperature range of 200–220 °C, beyond which the strength of these alloys degrades rapidly due to reversion and coarsening of the strengthening precipitates [1–3]. For higher-temperature applications, steel and titanium alloys are widely utilized. The high demand for low-density components in transportation systems necessitates the design and fabrication of lightweight Al alloys for high-temperature applications (e.g., in and near engines and brakes),

which remain strong for long exposure times at elevated temperatures. In coarse-grained Al alloys, micro-alloying additions of Sc (<0.3 at.%) result in significant improvements in creep and coarsening resistance up to 400 °C, due to the formation of nanoscale, coherent Al_3Sc -based (L_{12} -structure) precipitates [4–10]. The high number density ($10^{22}\text{--}10^{24} \text{ m}^{-3}$) of coherent precipitates achievable in these alloys also inhibits the migration of grain boundaries due to the Zener-drag effect, resulting in a high recrystallization resistance [11–14]. Additionally, Mg can be added to reduce the Al–Sc alloy density and provide solid-solution strengthening, resulting in an increase in density-normalized properties [15–20].

The objective of the present research is to study the microstructural evolution of an Al–Mg–Sc alloy subjected

* Corresponding author. Tel.: +1 847 491 3575.

E-mail address: voquynhon@gmail.com (N.Q. Vo).

to friction-stir processing (FSP) at the subnanoscale level using atom probe tomography (APT). FSP is a solid-state joining technology patented by The Welding Institute (TWI) [21]. It involves advancing a rotating hard pin, normally made of steel, between two contacting metal pieces if joining is desired, or within a monolithic metal piece to alter its microstructure [22,23]. In the former case, joined regions are heated by frictional forces and deformed plastically by the rotating pin. FSP joins efficiently Al alloy parts without melting them [22]. Due, however, to the high temperatures involved in this process (up to 400–500 °C), most Al alloys lose some or all of their strength as their strengthening precipitates coarsen and/or dissolve [12,24,25]. Transmission electron microscopy (TEM) has been widely utilized to study the microstructure of FSP samples of Al alloys [22,23], while APT has been utilized to a limited extent [26].

In prior studies of the same Al–Mg–Sc material [27,28], FSP resulted in substantial grain refinement of a cast alloy, which effectively strengthens it by grain boundaries due to the Hall–Petch effect. High-temperature heat treatments altered neither its microstructure nor its strength. Although the positive effects of Al₃Sc precipitates were postulated, their exact strengthening contribution remained unclear. To achieve a better understanding, precipitate radii, number density, and morphology for different FSP and aging conditions need to be measured. We have measured the above parameters utilizing APT and calculated strength increments in the FSP region due to precipitation strengthening, which are then compared to experimental microhardness measurements in the light of the concomitant grain size strengthening.

2. Experimental procedures

A 3.75 mm thick sheet of twin-roll-cast (TRC) Al–Mg–Sc alloy with a nominal composition of Al–4.1Mg–0.47Sc–0.022Zr–0.041Ti–0.15Fe–0.043Si, wt.% (Al–4.5 Mg–0.28Sc–0.007Zr–0.02Ti–0.07Fe–0.04Si, at.%) produced at CSIRO, Australia, was subjected to single-pass FSP at Missouri University of Science and Technology. Details of the friction-stir tool and processing are published elsewhere [22,23,29]. Specifically, an FSP tool is made of a step-spiral tool steel. The shoulder diameter and pin height are 12.0 and 2.20 mm, respectively. The pin diameter at the tip and the shoulder end (root) are 3.75 and 6.00 mm, respectively. Two different tool rotational rates – 325 and 400 rpm – were utilized and the resulting samples are labeled F325 and F400. The tool traverse speed was 3.4 mm s⁻¹ (8 inch min⁻¹) and the tilt angle of the tool, 2.5°, was constant during FSP processing.

Vickers microhardness measurements were performed with a Duramin-5 microhardness tester (Struers) using a 300 g load applied for 10 s on a cross-section of the sample, perpendicular to the surface and the tool direction and ~1.2 mm below the surface, polished to a 1 μm surface finish. Primary precipitates on the polished surface were

imaged by scanning electron microscopy (SEM) using a Hitachi S-4800-II microscope, equipped with an Oxford INCAx-act detector for energy-dispersive X-ray spectroscopy (EDS). Electron backscatter diffraction (EBSD) was performed to measure grain diameters.

Specimens for three-dimensional (3-D) local-electrode atom probe (LEAP) tomography were prepared by cutting blanks with a diamond saw to $\sim 0.35 \times 0.35 \times 10$ mm³. These samples were then electropolished at 20–25 V dc using a solution of 10% perchloric acid in acetic acid, followed by electropolishing at 12–18 V dc employing a solution of 2% perchloric acid in butoxyethanol; both were performed at room temperature. Pulsed-voltage and pulsed-laser APT were performed using a LEAP 4000X Si-X tomograph (Cameca, Madison, WI) [30,31] at a specimen temperature of 30 K. For the pulsed-voltage mode, a pulse fraction (pulse voltage/steady-state dc voltage) of 20% and a pulse repetition rate of 200 kHz were utilized. For pulsed-laser dissection, focused picosecond ultraviolet (UV) laser pulses (wavelength = 355 nm) with a laser beam waist of <5 μm at the e⁻² diameter were employed. A laser energy of ~0.075 nJ per pulse and a pulse repetition rate of 500 kHz were utilized. LEAP tomographic data were analyzed employing IVAS v3.6 (Cameca Instruments). The matrix/precipitate interfaces were delineated with Sc iso-concentration surfaces. The measurement errors for all quantities were calculated based on counting statistics and standard error propagation techniques [32]. A typical mass-to-charge state (m/n) spectrum is displayed in Fig. 1. The three isotopes of Mg are doubly charged at 12, 12.5 and 13 amu: their isotopic abundances are 78.4 ± 0.3% for ²⁴Mg²⁺, 10.5 ± 0.3% for ²⁵Mg²⁺ and 11.1 ± 0.3% for ²⁶Mg²⁺, which are in agreement with the handbook values. Sc is also doubly charged at 22.5 amu and it is known to form multiple hydrides [33], which possibly overlap with singly charged Mg peaks at 24, 25 and 26 amu. Based, however, on the integrated peak ratio, which should match their isotopic abundances, singly charged Mg is readily distinguished from Sc hydrides.

The measured matrix Sc concentration in the as-cast alloy (referred to as parent alloy), far away from the stir zone, is displayed in Fig. 2 as a function of laser energy. The dashed line indicates the results of a bulk chemical analysis performed by direct current plasma mass spectrometry (DCPMS, ATI Wah Chang, Albany, OR). The point at 0 nJ corresponds to a dataset collected using voltage pulsing at a pulse fraction of 20%. Fig. 2 demonstrates that the measured Sc concentration is consistent with the DCPMS result and relatively insensitive to the laser-pulse energy through 0.15 nJ per pulse. Voltage pulsing results in a ~20% overestimation of the Sc concentration in the matrix.

The desorption pattern recorded during an APT analysis, which is the two-dimensional image of the recorded positions of all arrival ions on the detector, for an Al alloy microtip sometimes exhibits a pole structure, containing crystallographic information about the material. This method has been utilized to study defects and grain bound-

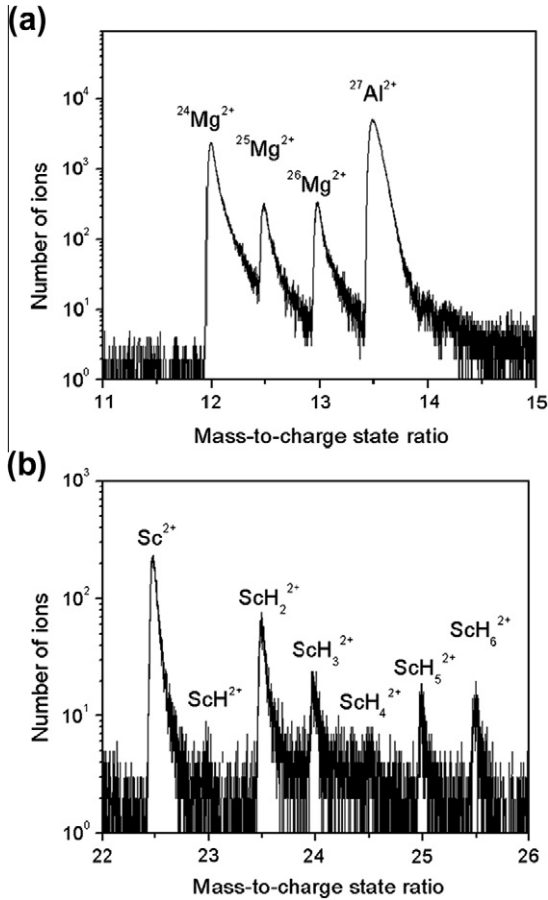


Fig. 1. Example of mass-to-charge state ratio spectrum from an atom probe tomographic (APT) microtip.

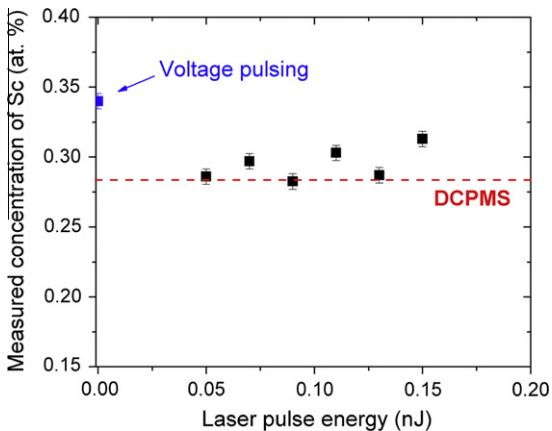


Fig. 2. Measured concentration of Sc as a function of laser pulse energy for the as-cast sample, using a picosecond ultraviolet laser with a 355 nm wavelength. The analysis temperature was ~ 30 K. The point at 0 nJ corresponds to a data set collected using voltage pulsing without a laser, at a pulse fraction (pulse voltage/steady state DC voltage) of 20%. The effective pulse fraction for laser pulsing is 20%. The dashed line indicates the results of a bulk chemical analysis using direct current plasma mass spectrometry.

aries employing field-ion microscopy [34–36]. The APT desorption pattern was utilized in the current investigation to reveal grain boundaries in the FSP Al alloy.

3. Results

3.1. SEM and Vickers hardness

The as-cast and FSP samples were examined by SEM. Fig. 3 indicates the presence of primary precipitates with two different size distributions, a few micrometers and a few tens of micrometers in diameter, respectively. EDS measurements indicate that, besides Al, these precipitates contain Mg, Fe and Sc for the smaller ones, and Sc, Ti and Zr for the larger ones. The latter precipitates, which probably correspond to $\text{Al}_3(\text{Sc}, \text{Zr}, \text{Ti})$ primary precipitates created on solidification and/or on subsequent cooling during the twin-roll-casting operation, are also present in the friction-stir zone. The high temperature and plastic strain ($\epsilon \sim 5$) are sufficient to dissolve the fine precipitates, but not the coarser ones [37]. It is possible, however, that the latter precipitates dissolve at peak temperature during FSP processing before re-precipitating upon cooling to ambient temperature.

Vickers microhardness values measured across the friction-stir zone of the four studied samples are displayed in Fig. 4a and b. The microhardness values for the as-cast and peak-aged heat treatment (290 °C for 22 h; hereafter referred to as peak-aged samples) regions outside the FSP zone are 800 ± 17 and 1350 ± 35 MPa, respectively. The high strength of the as-cast sample is mainly due to Mg solid-solution strengthening. Additional strengthening of the peak-aged sample is due to Al_3Sc (L_{12})-based precipitate strengthening. Quantitative strength contributions from different strengthening mechanisms are discussed in Section 4.1.

An increase of microhardness with respect to the as-cast values is observed within the friction-stir zone for both rotational tool speed conditions (Fig. 4a and b). Microhardness is nearly constant across the friction-stir zone at 1040–1110 MPa for F400 and 1200–1300 MPa for F325. The width of the friction-stir zone is somewhat wider for F400 than for F325 (7 vs. 4 mm). The strengthening mechanisms in both samples are grain-boundary and Al_3Sc precipitate strengthening, as described quantitatively in Section 4.1.

The microhardness of the F325 sample within the friction-stir zone is essentially unchanged before and after peak aging, and exhibits a shallow gradient of ~ 100 MPa between the advancing and retreating side zones, Fig. 4a. For the F400 sample, in contrast, additional strengthening is observed after peak aging: the microhardness value is unchanged on the advancing side, but is ~ 250 MPa higher on the retreating side at the friction-stir zone/parent interface. The microhardness values have thus a gradient, ranging from ~ 1070 to 1330 MPa from the advancing to retreating side of the tool, respectively, rather than being symmetric with respect to the centerline of the friction-stir zone as in the case before peak-aging.

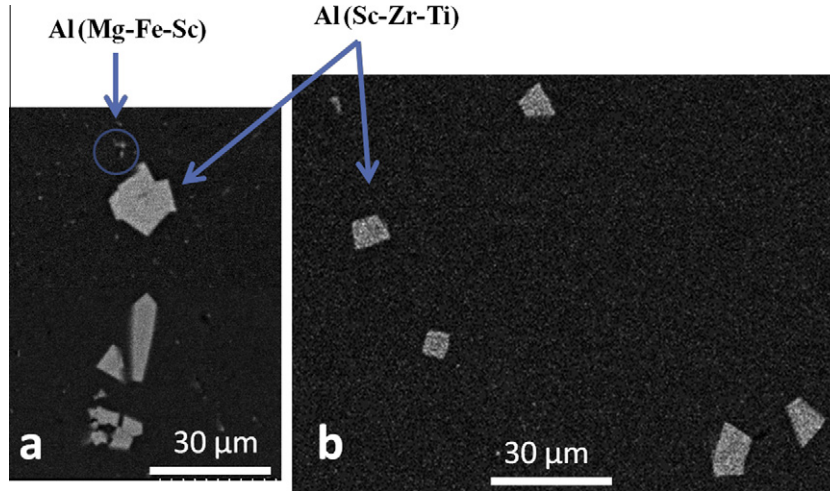


Fig. 3. Scanning electron microscope micrographs of: (a) as-cast state and (b) state after friction-stir processing (F400), showing the two types of primary precipitates present, Al(Mg-Fe-Sc) and Al(Sc-Zr-Ti).

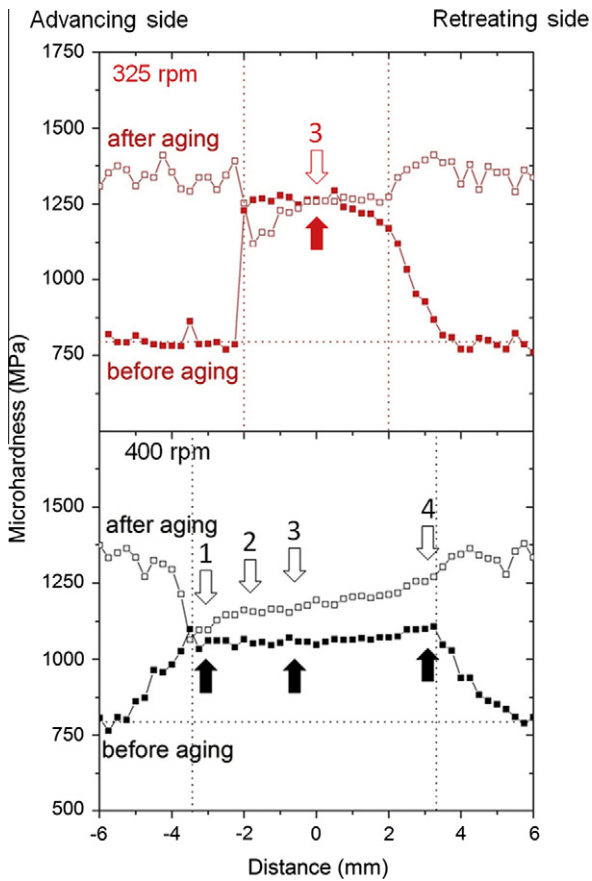


Fig. 4. Vickers microhardness across the stir zone (between vertical dotted lines) for: (a) sample F325 and (b) sample F400. Arrows are sample locations, where microstructures were studied by atom probe tomography.

3.2. Microstructural evolution

3.2.1. As-cast and peak-aged parent alloy

In the as-cast state, Mg and Sc appear qualitatively to be homogeneously distributed in the α -Al (face-centered cubic,

fcc) matrix, Fig. 5. Based on the APT mass-to-charge-state spectra, Fig. 1, other elements in the α -Al matrix are below a conservative detection limit of ~ 20 at. ppm, which is significantly below the nominal concentrations of the elements comprising the alloy (70 Zr, 200 Ti, 700 Fe, 400 Si at. ppm). Therefore, these elements are most likely concentrated in the primary precipitates displayed in Fig. 3. In addition to not being detected in the as-cast sample they are also not detected in any of the other APT samples.

Precipitates are observed after peak-aging the sample, far away from the friction-stir zone, at 290 °C for 22 h, Fig. 6. A cluster-search algorithm with a maximum separation distance of 1.5 nm was used to identify Sc atoms within precipitates, assuming they are all spherical: 200 precipitates were identified and analyzed. The average precipitate composition is 17.2 ± 0.2 at.% Sc, Fig. 7a. The average precipitate radius, $\langle R \rangle$, and number density, N_v ,

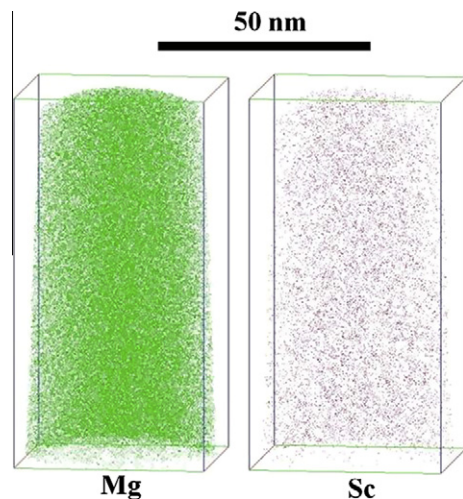


Fig. 5. 3-D reconstruction of an analyzed atom probe tomographic volume, which contains $\sim 9 \times 10^6$ atoms, displaying all Mg and Sc atoms, from an as-cast specimen.

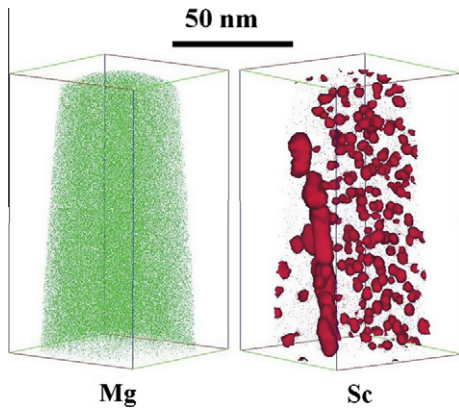


Fig. 6. 3-D reconstruction of an atom probe tomographic volume, containing $\sim 10 \times 10^6$ atoms, displaying all Mg and Sc atoms. A 2 at.% Sc isoconcentration surface is employed to delineate the Al_3Sc (L_{12} structure) precipitates. The dataset is from a cast specimen peak-aged at 290 °C for 22 h, ~ 25 mm away from the stir zone edge.

are 1.5 ± 0.4 nm and $8.0 \pm 0.6 \times 10^{23} \text{ m}^{-3}$, respectively, and the volume fraction, ϕ , is 1.10%. A normalized precipitate size distribution (PSD) is displayed in Fig. 7b. Mg atoms are also present within the precipitates at an average concentration of 4.16 at.%, which is greater than the 3.64 at.% average value in the matrix, Fig. 7a. The presence of Mg within the Al_3Sc (L_{12}) precipitates is a kinetic phenomenon and not a thermodynamic effect: Marquis and Seidman [33] observed a similar structure in an Al–0.12 Sc–2.2 Mg at.% alloy aged at 300 °C. Mg atoms were most likely involved in the heterogeneous nucleation of Al_3Sc precipitates due to an attractive binding energy between Mg and Sc atoms [17,33]. As the Al_3Sc (L_{12}) precipitates grow, Mg atoms are kinetically trapped within the Al_3Sc precipitates because the diffusivity of Mg in an ordered structure (L_{12}) is strongly correlated and significantly smaller than in a random fcc solid solution.

Fig. 7a displays a proximity histogram [38] that shows the average composition in shells of 0.1 nm thickness at a given distance from the average $\alpha\text{-Al}/\text{Al}_3\text{Sc}$ (L_{12}) interface defined by an isoconcentration surface at 12 at.% Sc. The relative Mg concentration enhancement at the interface is $\sim 25\%$, which is localized within 2 nm of this interface. The existence of Mg atoms within the Al_3Sc (L_{12}) precipitates is consistent with Mg-rich clusters being involved during their nucleation.

3.2.2. Friction-stir processing at 400 rpm

Microstructures at different locations across the friction-stir zone of the F400 sample were studied employing APT. These locations are indicated in Fig. 4 in the conditions before (solid arrow) and after (open arrow) peak-aging. Locations are labeled from 1 through 4 from the advancing side to the retreating side. 3-D reconstructions of analyzed volumes, displaying only Sc atoms and 3 at.% Sc isoconcentration surfaces of the F400 sample, are shown in Fig. 8. At some locations, more than one sample was

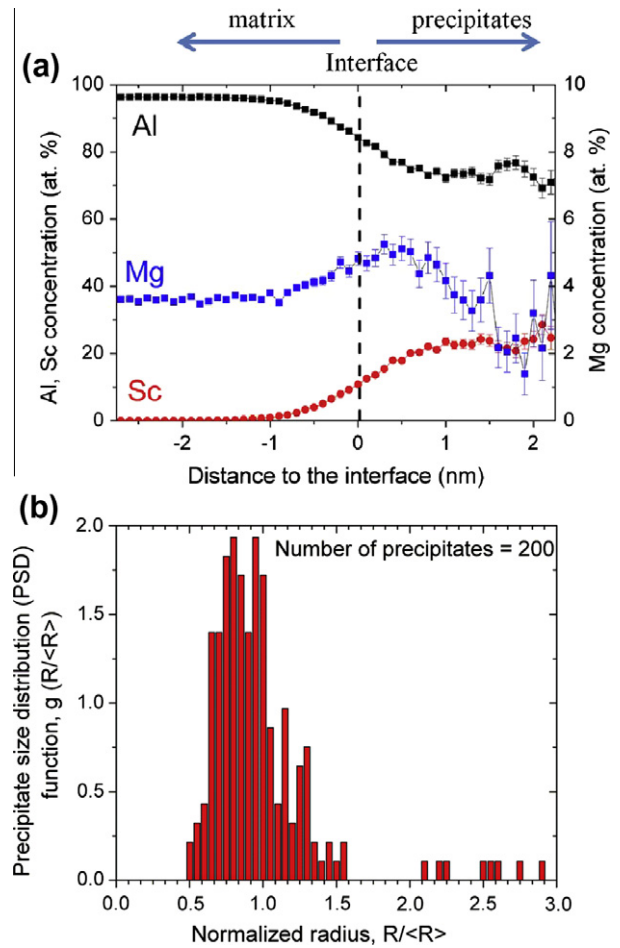


Fig. 7. (a) Proximity histogram concentration profiles across the matrix/precipitate interface exhibiting Mg segregation at the $\alpha\text{-Al}/\text{Al}_3\text{Sc}$ interface and (b) Al_3Sc precipitate size distribution (PSD) function vs. the normalized radius, from a specimen peak-aged at 290 °C for 22 h, ~ 25 mm away from the stir zone edge (elongated precipitates, Fig. 6, are excluded from this calculation).

studied by APT to improve the counting statistics. Large Al_3Sc precipitates with an average radius in the range 10–25 nm were observed at locations 2 and 3. Radii of precipitates not fully contained within the analyzed volume were estimated by measuring radii of extrapolated precipitates, assuming they have symmetrical morphology. Some precipitates display a lobed-cuboid morphology rather than a spherical morphology. At location 2, ϕ and N_v are 0.90% and $1.0 \pm 1.0 \times 10^{21} \text{ m}^{-3}$, respectively, and at location 3, these values are 0.50% and $1.5 \pm 2.1 \times 10^{21} \text{ m}^{-3}$, respectively. Although no Al_3Sc precipitates are observed at location 1, precipitates are anticipated to exist because the matrix Sc concentration is lower than in the parent matrix (0.05 at.%). The average precipitate edge-to-edge distance is, therefore, larger than the maximum distance, ~ 120 nm, in the analyzed volume dimensions ($70 \times 70 \times 60 \text{ nm}^3$). The precipitate volume fraction, ϕ , at this location is estimated to be $\sim 0.92\%$. The Sc supersaturation at location 4 is the same as in the parent matrix, 0.28 at.%; therefore, no precipitates are present. Values of the Sc concentration of all samples studied are displayed

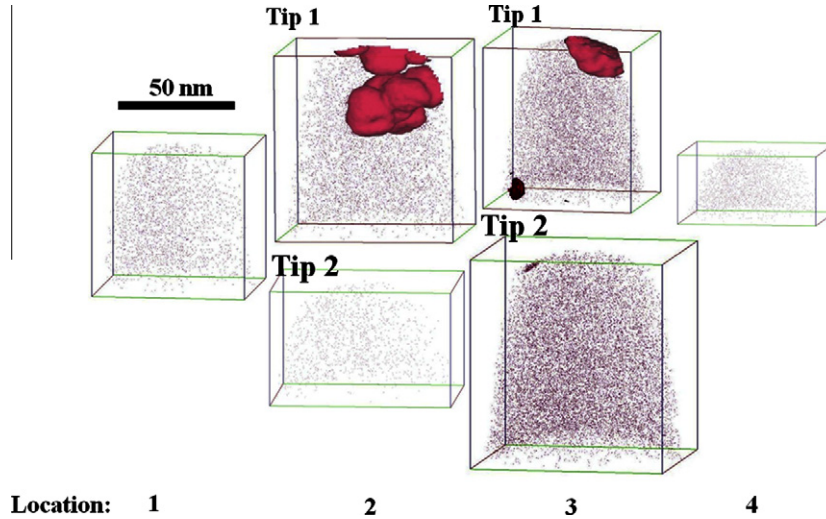


Fig. 8. 3-D reconstruction of atom probe tomographic volumes at different locations within the friction-stir zone of sample F400, before aging. Only Sc atoms (100%) are displayed, and the isoconcentration surfaces are for ~ 3 at.% Sc. Volumes contain: 7×10^6 atoms (location 1), 11×10^6 atoms (location 2, tip 1), 5×10^6 atoms (location 2, tip 2), 5×10^6 atoms (location 3, tip 1), 13×10^6 (location 3, tip 2) and 1.5×10^6 atoms (location 4).

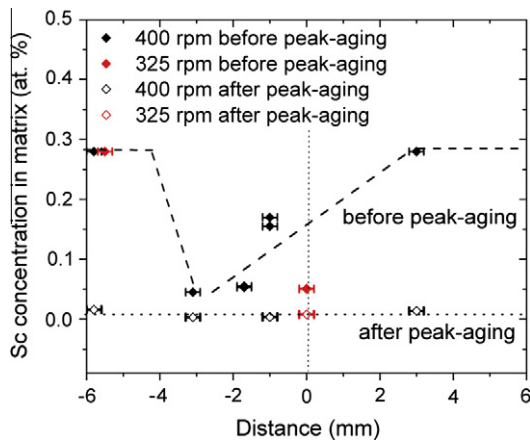


Fig. 9. Sc concentration in α -Al matrix across the friction-stir zone, for sample F400 (black symbols) and F325 (red symbols) before aging (solid symbols) and after aging (open symbols) at 290 °C for 22 h. (For interpretation of the references to color in this figure legend, the reader is referred to the web version of this article.)

in Fig. 9. The Sc concentration is almost the same as the Sc supersaturation because the solubility of Sc in the α -Al matrix is negligible at room temperature (7×10^{-9} at.%) and 290 °C (1.36×10^{-3} at.%) [39]. Thus, the Sc-supersaturation value will be used hereafter. For F400, it is somewhat surprising that these values appear to exhibit a gradient from the advancing to retreating side.

3.2.3. Friction-stir processing at 400 rpm after peak-aging

3-D reconstructions of the analyzed volumes, displaying only Sc atoms and 3 at.% Sc isoconcentration surfaces, are displayed in Fig. 10 for the F400 sample after peak-aging. Al_3Sc precipitates are observed at all locations except at location 1 for a $40 \times 40 \times 90 \text{ nm}^3$ volume. The precipitates display different morphologies: spherical, lobed and platelet-like. At location 3 the average radius, ϕ , and N_v are $20.3 \pm 10.6 \text{ nm}$, 1.10% and $2.7 \pm 1.9 \times 10^{21} \text{ m}^{-3}$, respectively. The values of the Sc supersaturation of all studied peak-aged samples are displayed in Fig. 9. Because of the

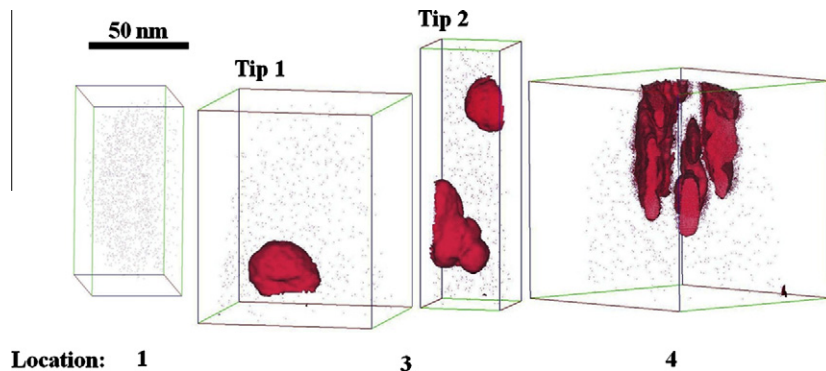


Fig. 10. 3-D reconstruction of volumes at different locations within the friction-stir zone of sample F400, after aging at 290 °C for 22 h. Only the Sc atoms (100%) are displayed, and the isoconcentration surfaces are for ~ 3 at.% Sc. Volumes contain: 5×10^6 atoms (location 1), 15×10^6 atoms (location 3, tip 1), 5×10^6 atoms (location 3, tip 2) and 15×10^6 atoms (location 4).

concentration gradient of the Sc supersaturation across the friction-stir zone observed in the F400 sample before peak-aging, the additional precipitate volume fractions resulting from post-aging also have a gradient: 0.20% at location 1, 0.60% at location 3 and 1.10% at location 5. The precipitate volume fraction gradient is anticipated to be the primary reason for the gradient in microhardness increase within the friction-stir zone. Al_3Sc precipitates at location 4 appear to have a platelet-like morphology. The desorption pattern of the ATP analysis of this sample, Fig. 11a, displays two different sets of pole patterns, separated by a straight line. This line indicates the presence of a grain boundary, where the platelet-like precipitates are aligned

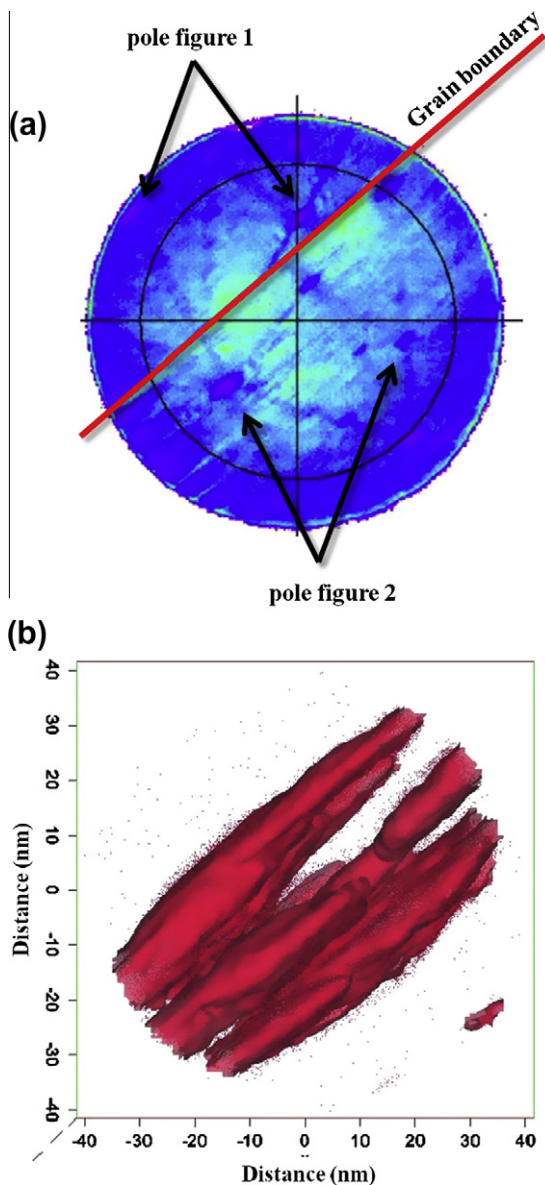


Fig. 11. (a) Desorption pattern during an atom probe tomographic analysis showing two sets of pole figures separated by a grain boundary, (b) cross-sectional view of atom probe tomographic 3-D reconstruction (Fig. 9) exhibiting platelet-like Al_3Sc precipitates along a grain boundary of the sample at location 4 of F400 sample after aging.

(Fig. 11b). This non-equilibrium precipitate morphology appears to be the result of heterogeneous nucleation and growth of precipitates at a grain boundary. The average grain diameter in the friction-stir zone of F400 sample is $0.73 \pm 0.44 \mu\text{m}$ [40]. The average length of an APT analyzed volume is a few tenths of a micrometer. The probability of an analyzed volume containing a grain boundary structure is thus high for this material.

3.2.4. Friction-stir processing at 325 rpm

3-D reconstructions of analyzed volumes, displaying only Sc atoms and a 3 at.% Sc isoconcentration surface, are displayed in Fig. 12 for the F325 sample. All detected Al_3Sc precipitates display a platelet-like morphology. Average platelet precipitate thickness and diameter are $6.8 \pm 4.6 \text{ nm}$ and $\sim 25 \text{ nm}$, respectively. The precipitate volume fraction, ϕ , and number density, N_v , are 0.92% and $1.1 \pm 0.5 \times 10^{22} \text{ m}^{-3}$, respectively. The average grain diameter in the friction-stir zone of the F325 sample is $0.49 \pm 0.23 \mu\text{m}$ [40], which is about half the value of the F400 sample. The total length of all the analyzed volumes is $0.23 \mu\text{m}$, which is about half of the average grain diameter: thus, there is a high probability that the analyzed volume contains a grain boundary. As discussed, the non-equilibrium precipitate morphology is interpreted to be the result of heterogeneous nucleation and growth of

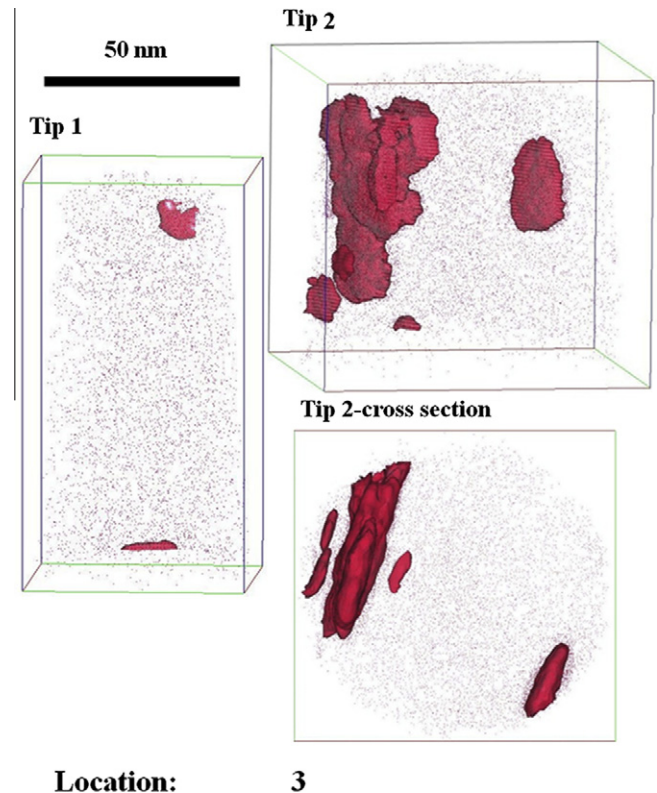


Fig. 12. 3-D reconstruction of volumes at location 3 within the friction-stir zone of sample F325, before aging. Only the Sc atoms (100%) are displayed, and the isoconcentration surfaces are for $\sim 3 \text{ at.}\%$ Sc. Volumes contain 8×10^6 atoms (tip 1) and 11×10^6 atoms (tip 2).

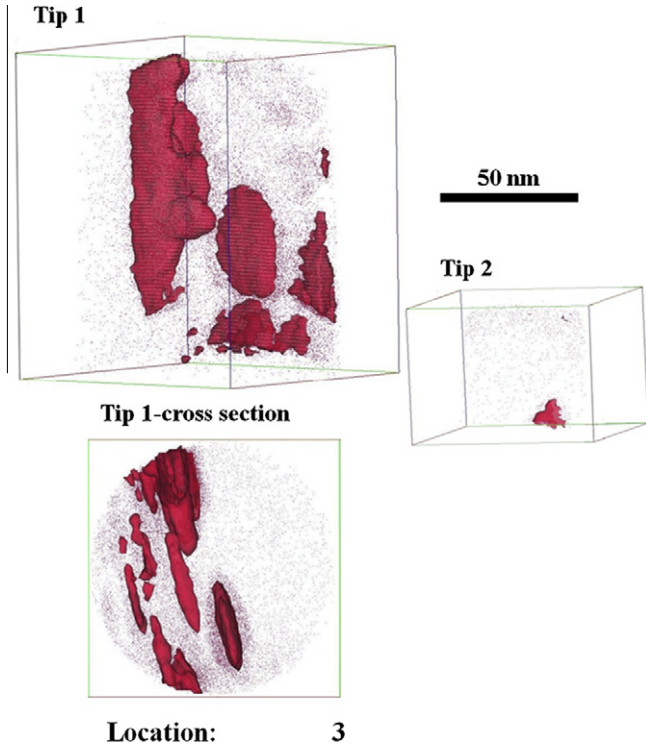


Fig. 13. 3-D reconstruction of volumes at location 3 within the friction-stir zone of sample F325, after aging at 290 °C for 22 h. Only the Sc atoms (100%) are displayed, and the isoconcentration surfaces are for ~3 at.% Sc. Volumes contain 21×10^6 atoms (tip 1) and 4×10^6 atoms (tip 2).

precipitates at grain boundaries. The Sc concentration remaining in the matrix is ~0.05 at.%, which implies that essentially all the Sc solute precipitated from the solid solution after FSP at 325 rpm.

3.2.5. Friction-stir processing at 325 rpm after peak-aging

3-D reconstructions of analyzed volumes of the F325 sample after peak-aging, Fig. 13, are similar to those before aging. All detected precipitates display a platelet-like morphology. The average platelet precipitate thickness and diameter are 4.9 ± 3.2 nm and >25 nm, respectively. The precipitate volume fraction, ϕ , and number density,

N_v , are 1.10% and $6.5 \pm 2.9 \times 10^{21} \text{ m}^{-3}$, respectively. Thus, post-aging at 290 °C for 22 h does not alter the microstructure of the F325 sample. This is consistent with the unchanged Vickers microhardness values between the pre- and post-aging states. The precipitate number density, N_v , volume fraction, ϕ , and average radius, $\langle R \rangle$, are listed in Table 1 for all experimental conditions.

4. Discussion

4.1. Strengthening mechanisms

4.1.1. Grain boundary strengthening

The yield strength, σ_y , is related to the average grain boundary diameter (D) by the Hall–Petch relationship:

$$\sigma_y = \sigma_0 + kD^{-1/2} \tag{1}$$

where σ_0 is the intrinsic resistance of the lattice to dislocation motion and k is an experimental constant describing the relative strengthening contribution from grain boundaries. In a dilute Al–Mg–Li alloy, k was determined to be $0.17 \text{ MN m}^{-3/2}$ [41]. The average grain diameters of the parent alloy, F400, and the F325 samples are 19 ± 27 , 0.73 ± 0.44 and $0.49 \pm 0.23 \mu\text{m}$, respectively. Using Eq. (1), the estimated ranges of yield strength strengthening of these three samples are 25–40, 157–316 and 200–333 MPa, respectively. The average grain diameters of these samples were unchanged after the peak-aging heat treatment.

4.1.2. Solid-solution strengthening

The yield strength increment $\Delta\sigma_y$ due to solid-solution strengthening is:

$$\Delta\sigma_y = \frac{3.1\omega Gc^{1/2}}{700} \tag{2}$$

where ω is an experimental constant, G is the shear modulus of the α -Al matrix, c is the concentration of solute in at.% [42], and the shear modulus of Al is 25.4 GPa at room temperature [43]. The Mg atomic concentration, which is

Table 1

Al₃Sc precipitate number density, volume fraction and average radius (average thickness and diameter are also given for platelet-like Al₃Sc precipitates). Number of counted precipitates in each sample is included. Data for FSP samples (3rd to 6th data column) are from the center of the FSP zone.

	TRC ^a	TRC + age	400 rpm	400 rpm + age	325 rpm	325 rpm + age
Number of precipitates	0	200	0.5	2	5	5
Number density (m^{-3})	–	$8.0 \pm 0.6 \times 10^{23}$	$1.5 \pm 2.1 \times 10^{21}$	$2.7 \pm 1.9 \times 10^{21}$	$1.1 \pm 0.5 \times 10^{22}$	$6.5 \pm 2.9 \times 10^{21}$
Volume fraction (%)	–	1.10	0.50	1.10	0.92	1.10
Radius (nm)	–	1.5 ± 0.4	10–25	20.3 ± 10.6	8.1^b	$>7.3^b$
Thickness (nm)	–	–	–	–	6.8 ± 4.6	4.9 ± 3.2
Diameter (nm)	–	–	–	–	25	>25
Calculated strength increase from precipitation (MPa)	–	247	30–58	54	94	<111

^a Twin-roll cast.

^b Effective spherical radii (R_{eff}) of platelet-like Al₃Sc precipitates were calculated as $R_{\text{eff}} = 1/2(\text{thickness} \times \text{diameter} \times \text{diameter})^{1/3}$, which mimics the calculation of an effective ellipsoid radius [65].

the main solid-solution strengthener in the current alloy, is ~ 3.5 – 4.0 at.%, based on the LEAP tomographic analyses; ω is estimated to be 0.4 for Mg in the Al–Mg alloy [3,44]. Since the Mg solute atoms are assumed to be homogeneously distributed in the α -Al matrix, the yield strength increase due to Mg solid-solution strengthening calculated from Eq. (2) is 85–95 MPa.

4.1.3. Precipitate strengthening

Precipitate strengthening results from order strengthening, coherency strengthening, modulus mismatch strengthening and Orowan dislocation looping. Relationships for the yield strength increments from each of these contributions of Al_3Sc precipitate in α -Al matrix are from Refs. [6,45]. The order strengthening, $\Delta\sigma_{ord}$, is given by:

$$\Delta\sigma_{ord} = 0.81M \frac{\gamma_{APB}}{2b} \left(\frac{3\pi\phi}{8} \right)^{1/2} \quad (3)$$

In this equation, $M = 3.06$ is the mean matrix orientation factor for Al [46], $b = 0.286$ nm is the magnitude of the matrix Burgers vector [43], ϕ is the volume fraction of precipitates and $\gamma_{APB} = 0.5 \text{ J m}^{-2}$ is an average value of the Al_3Sc anti-phase boundary (APB) energy for the (111) plane [47–49].

The coherency strengthening $\Delta\sigma_{coh}$ is given by:

$$\Delta\sigma_{coh} = M\alpha_c (G\theta)^{3/2} \left(\frac{\langle R \rangle \phi}{0.5Gb} \right)^{1/2} \quad (4)$$

where $\alpha_c = 2.6$ is a constant [50], $\langle R \rangle$ is the average precipitate radius, and $\theta = 0.83\%$ [51] is the constrained lattice parameter mismatch at room temperature.

The modulus mismatch strengthening, $\Delta\sigma_{mod}$, is given by:

$$\Delta\sigma_{mod} = 0.0055M(\Delta G)^{3/2} \left(\frac{2\phi}{Gb^2} \right)^{1/2} b \left(\frac{\langle R \rangle}{b} \right)^{(3m-1)}; \quad (5)$$

where $\Delta G = 42.5$ GPa is the shear modulus mismatch between the matrix and the Al_3Sc precipitates [52], and m is a constant taken to be 0.85 [50].

Finally, strengthening due to Orowan dislocation looping $\Delta\sigma_{Or}$ is given by:

$$\Delta\sigma_{Or} = M \frac{0.4}{\pi} \frac{Gb}{\sqrt{1-\nu}} \frac{\ln \left(\frac{\sqrt{2/3}\langle R \rangle}{b} \right)}{\lambda} \quad (6)$$

where $\nu = 0.34$ is Poisson's ratio for Al [46]. The inter-precipitate distance, λ , is taken to be the square lattice spacing in parallel planes, which is given by [53]:

$$\lambda = \left[\left(\frac{3\pi}{4\phi} \right)^{1/2} - 1.64 \right] \langle R \rangle \quad (7)$$

Precipitate strengthening is determined by the minimum value of $\Delta\sigma_{ord}$, $\Delta\sigma_{coh} + \Delta\sigma_{mod}$ and $\Delta\sigma_{Or}$. The first three strengthening mechanisms dominate at small radii, and

the Orowan dislocation looping mechanism, $\Delta\sigma_{Or}$, dominates for larger radii.

4.1.4. Strengthening by dislocations

The yield strength increment, $\Delta\sigma_{dis}$, due to dislocations, i.e., work-hardening, is given by [54]:

$$\Delta\sigma_{dis} = M\alpha_d Gb\sqrt{\rho}, \quad (8)$$

where α_d is a material-dependent constant in the range of 0.15–0.5 [54] and ρ is the dislocation density. Within the friction-stir zone, recrystallization and possibly recovery are clearly observed. The grain diameter is decreased from 19 μm in the as-cast state to 0.73 and 0.49 μm in the stir zone for the two rotational tool-speed conditions, respectively. Hence, a low dislocation density is anticipated, and thus work-hardening can be ignored within the stir zone. Similar observations of the reduction of dislocation density due to recrystallization and recovery in friction-stirred zones have been reported [55,56]. The existence of a dislocation density gradient is possible across the stir zone and has, in fact, been reported [22,57]. Its contribution to the microhardness gradient should, however, be negligible since the observed microhardness across the stir zone is relatively uniform in both FSP samples before peak-aging, Fig. 4. Therefore in this article, we assume that strengthening by dislocations is negligible at different locations and after different processing stages. Detailed dislocation density distributions and their effects on strength are, however, worthwhile subjects for future research.

The strengthening contributions from solid-solution hardening, grain boundaries and precipitate strengthening for all conditions are listed in Table 2. Data for FSP samples were recorded at the center of the friction-stir zone. The total predicted yield strength, which is taken as the linear sum of the solid solution, grain boundary and precipitate strengthening contributions [58], and the strength of pure Al (60 MPa [59]), is in good agreement with the experimental microhardness values. This suggests that there are negligible interactions among the strengthening mechanisms in the alloy we studied. Good agreement between the predictions of the above equations and the measured microhardnesses has been found in many Al–Sc-based alloys [15,44,60].

The predicted strengths for the as-cast and peak-aged parent alloy (outside the friction-stir zone) are slightly underestimated compared to the experimental values. Potential additional strengthening sources include work-hardening and primary precipitates. A high strengthening increment after aging (247 MPa calculated and 183 MPa ($\Delta H/3$) experimental value) reflects the high number density, $8.0 \times 10^{23} \text{ m}^{-3}$, of nanoscale Al_3Sc precipitates. It is achieved using the maximum Sc supersaturation in the α -Al matrix and the heterogeneous nucleation of Al_3Sc precipitates caused by the presence of Mg.

The range of predicted strengths of FSP samples, for both rotational tool speeds, pre- and post-aging, agree with

Table 2

Calculated strengthening contributions and yield strength, compared to experimental yield strength. Data for FSP samples (3rd to 6th data column) are from the center of the friction-stir zone and all values are in MPa.

	TRC ^a	TRC + age	400 rpm	400 rpm + age	325 rpm	325 rpm + age
Mg solid solution strengthening (Eq. (2))	85–95	85–95	85–95	85–95	85–95	85–95
Grain boundary strengthening (Eq. (1))	25–40	25–40	157–316	157–316	200–333	200–333
Precipitate strengthening (Eqs. (3)–(7))	0	247	30–58	54	94	0–111
Total predicted yield strength ^b	170–195	417–442	332–529	356–525	439–582	345–599
Experimental yield strength ^c	266 ± 6	450 ± 12	380	417	450	465

^a Twin-roll cast.

^b Sum of three contribution and strength of pure Al ($\sigma_0 = 60$ MPa [59]).

^c Calculated as $HV/3$.

the experimental values. Experimental values are, however, on the low side of the predicted range of strength. This suggests that the strengthening contributions from grain boundaries and precipitates are overestimated. This may be due to the fact that we are fitting data for an Al–Mg–Li alloy to estimate the k parameter for grain-boundary strengthening of the present Al–Mg–Sc alloy. As most Al_3Sc precipitates are anticipated to nucleate and grow at grain boundaries, whereas precipitate strengthening (Orowan dislocation looping) calculations assume homogeneously distributed precipitates in the α -Al matrix, this assumption also introduces an error. Additionally, the fact that the experimental strengths of the F400 samples from locations 1–4 have the same value, whereas the precipitate volume fractions vary from $\sim 0.0\%$ to 0.92% , confirms that precipitate strengthening is negligible in this sample. Different precipitate morphologies, such as the platelet-like precipitates observed in F325, may also contribute to the deviation between predicted and experimental values.

The strengthening gradient in the F400 sample, after aging, appears to be the result of the asymmetric Sc supersaturation at different locations within the friction-stir zone, where the yield strength ($HV/3$) increase is in the range of 0–72 MPa. The increment in precipitate volume fraction, due to post-aging, is in the range of 0.20–1.10%. Taking the average precipitate radius after FSP to be 15 nm and assuming it changes negligibly due to post-aging implies that the predicted yield strength increase due solely to the increase of precipitate volume fraction is in the range of 6–67 MPa, which is in agreement with the experimental values. Varying dislocation density, resulting in work-hardening, at different locations within the stir zone could also contribute to the strengthening gradient. As noted, this contribution should, however, be negligible, especially after the further peak-aging treatment, where dislocations are annihilated. The microstructural and strength asymmetry in FSP of Al alloys was also observed in earlier studies. For example, Mahoney et al. [61] measured a variation in grain size from the advancing side to the retreating side in the FSP stir zone of 7050Al. Additionally, Zhao et al. [62] observed a microhardness gradient from the advancing side to the retreating side in the FSP stir zone of an Al–Mg–Sc alloy, as in the current results. Although these studies show an asymmetry in FSP stir zone of Al alloys, its

physical explanation is unclear and warrants future investigations.

4.2. Precipitate morphology

The non-equilibrium lobed-cuboidal morphology was observed earlier in dilute Al–Sc and Al–Sc–Zr alloys, where the Sc concentration is <0.18 at.%, and attributed to a small solute supersaturation [5,63,45]. Marquis et al. surmised that at low Sc supersaturations, the number density of precipitates is small ($<10^{21} \text{ m}^{-3}$) and precipitate growth occurs in a supersaturated matrix before the diffusional concentration fields commence overlapping. This results in a precipitate morphology that is determined by the growth kinetics. In the present case, the Sc supersaturation is higher (~ 0.30 at.%), and with a rapid increase of temperature to 400–500 °C due to FSP [22,24] and concomitant fast diffusion along dislocations and grain boundaries produced during FSP, a similar phenomenon is expected to occur. This phenomenon is also observed in the peak-aged parent alloy, Fig. 6, where several elongated precipitates are aligned along a plane, that is, a grain boundary, and whose diameter is much larger than the precipitates that form in the surrounding matrix. Elongated $Al_3(Sc,Zr)$ precipitates were also observed in an earlier study of rolled 5754Al with additions of 0.14 at.% Sc and 0.07 at.% Zr [64].

We finally consider the heterogeneous nucleation and growth of Al_3Sc precipitates in the FSP zones. FSP involves a heat input from the frictional forces and dynamic recrystallization processes occurring within the friction-stir zone. For a traverse tool speed of 3.4 mm s^{-1} , the temperature of the friction-stir zone is expected to increase to 400–500 °C within a few seconds [25], which provides Sc with sufficient mobility for precipitation and growth. Dynamic recrystallization introduces simultaneously dislocation networks, sub-grains and grain boundaries, which act as short-circuit diffusional paths for Sc. Therefore, FSP should result in heterogeneous nucleation and growth of Al_3Sc precipitates for these diffusional paths, which explains the rapid growth of precipitates ($\langle R \rangle = 10\text{--}20 \text{ nm}$) in the friction-stir zone. The existence of dislocations and grain boundaries with a high interface-to-volume ratio explains the additional precipitation of Al_3Sc after aging, which is also highly heterogeneous.

The short-circuit diffusional paths result in Sc atoms arriving at existing precipitates, rather than nucleating new Al_3Sc precipitates, which results in a negligible change in $\langle R \rangle$ and N_v . For example, locations 4 in the parent alloy and the F400 samples have the same Sc supersaturation, but have completely different precipitate morphologies after the peak-aging treatment: a high number density of small precipitates ($\langle R \rangle = 1.5$ nm) and a low number density of large platelet-like precipitates (12 nm thick and >50 nm in diameter), respectively.

5. Summary and conclusions

The microstructures of a twin-roll cast aluminum alloy (Al–4.5Mg–0.28Sc–0.007Zr–0.02Ti–0.07Fe–0.04Si at.%) were investigated by atom probe tomography after friction-stir processing (FSP) at two different rotational tool speeds (325 and 400 rpm), before and after a subsequent peak-age heat treatment. The following conclusions are drawn:

- Only Mg and Sc solute atoms are present in the as-cast α -Al (fcc) matrix, while the other alloying elements (Zr, Ti, Fe and Si) and some Sc are scavenged by two types of primary micron-size precipitates, which are too large to contribute significantly to the alloy's strength.
- Upon peak-aging of the cast sample, a high number density, $8.0 \times 10^{23} \text{ m}^{-3}$, of Al_3Sc precipitates form, with an average radius of 1.5 ± 0.4 nm. Magnesium atoms are present in small concentrations throughout the precipitates, which tend to segregate at the α -Al/ Al_3Sc (L_{12} structure) interface. In agreement with precipitation-strengthening calculations, the Vickers microhardness of the peak-aged alloy achieves 1350 ± 35 MPa due to these precipitates.
- The microhardness of the stir zone after friction-stir processing at rotational tool speeds of 325 and 400 rpm (but before aging) is mainly due to grain-boundary strengthening (given the submicron grain size), and only slightly to precipitate strengthening, because of the large, spherical and non-spherical Al_3Sc precipitates with effective radii up to 25 nm. The strengthening contribution by dislocations is unclear but is expected to be negligible.
- After peak-aging, the strength of the stir zone at the low rotational tool speed (325 rpm) was unchanged because Sc had almost completely precipitated during friction-stir processing. In contrast, a microhardness increase was observed for the higher rotational tool speed (400 rpm) after peak-aging, but its profile is asymmetric. This asymmetry corresponds to an asymmetry in the Sc supersaturation, leading to a gradient in Al_3Sc precipitate volume fractions at different locations within the friction-stirred zone.
- Spherical, lobed-cuboid and platelet-like Al_3Sc precipitate morphologies are present in the friction-stir zone, both before and after peak-aging. The latter two morphologies are a sign of non-equilibrium growth of the precipitates.
- Nucleation and growth of Al_3Sc precipitates are heterogeneous during friction-stir processing and post-aging, as expected from the existence of dislocations and a large grain-boundary area-to-volume ratio.

Acknowledgements

This research was sponsored by the Boeing Company. APT was performed at the Northwestern University Center for Atom-Probe Tomography (NUCAPT). The LEAP tomography system was purchased and upgraded with funding from NSF-MRI (DMR-0420532) and ONR-DURIP (N00014-0400798, N00014-0610539 and N00014-0910781) grants. The authors also gratefully acknowledge the Initiative for Sustainability and Energy at Northwestern (ISEN) for grants to upgrade the capabilities of NUCAPT. They thank Prof. R.S. Mishra and Dr N. Kumar for performing the FSP processing, providing electron backscatter diffraction (EBSD) data and the alloys studied here; Dr D. Isheim for his assistance with LEAP tomography; Dr I. Blum for his assistance with the IVAS software; and Mr C. Huskamp (Boeing) and Dr K.K. Sankaran (Boeing) for many useful discussions.

References

- [1] Silcock J, Heal T, Hardy H. *J Inst Metals* 1953;54:82:239.
- [2] Meetham GW. *J Mater Sci* 1991;26:853.
- [3] Polmear IJ. *Light alloys: from traditional alloys to nanocrystals*. 4th ed. Amsterdam: Elsevier; 2006.
- [4] Toropova LS, Eskin DG, Kharakterova ML, Dobatkina TV. *Advanced aluminum alloys containing scandium*. London: Gordon & Breach; 1998.
- [5] Marquis EA, Seidman DN. *Acta Mater* 2001;49:1909.
- [6] Seidman DN, Marquis EA, Dunand DC. *Acta Mater* 2002;50:4021.
- [7] Royset J, Ryum N. *Int Mater Rev* 2005;50:19.
- [8] Drits ME, Ber LB, Bykov YG, Toropova LS, Anastas'eva GK. *Phys Met Phys Metall* 1984;57:1172.
- [9] Drits ME, Dutkiewicz J, Toropova LS, Salawa J. *Cryst Res Technol* 1984;19:1325.
- [10] Vlach M, Stulikova I, Smola B, Zaludova N, Cerna J. *J Alloys Compd* 2010;492:143.
- [11] Paris H, Sanders Jr TH, Riddle YW. In: *Proc ICAA-6*, vol. 1; 1998. p. 499–504.
- [12] Ocenasek V, Slamova M. *Mater Charact J*. 2001;47:157.
- [13] Nieh TG, Hsiung LM, Wadsworth J, Kaibyshev R. *Acta Mater* 1998;46:2789.
- [14] Ferry M, Hamilton NE, Humphreys FJ. *Acta Mater* 2005;53:1097.
- [15] Marquis EA, Seidman DN, Dunand DC. *Acta Mater* 2003;51:4751.
- [16] Marquis EA, Seidman DN, Asta M, Woodward C, Ozolins V. *Phys Rev Lett* 2003;91:036101.
- [17] Marquis EA, Seidman DN. *Surf Interface Anal* 2004;36:559.
- [18] Marquis EA, Seidman DN. *Acta Mater* 2005;53:4259.
- [19] Filatov YA, Yelagin VI, Zakharov VV. *Mater Sci Eng A* 2000;A280:97.
- [20] Watanabe C, Watanabe D, Monzen R. *Mater Trans* 2006;47:2285.
- [21] Thomas WM, Nicholas ED, Needham JC, Murch MG, Smith PT, Dawes CJ. In: *EPS*, editors. *Improvements relating to friction welding*. Cambridge: The Welding Institute; 1991.
- [22] Mishra RS, Ma ZY. *Mater Sci Eng R* 2005;50:1.
- [23] Ma ZY. *Metall Mater Trans A* 2008;39A:642.

- [24] Mahoney MW, Rhodes CG, Flintoff JG, Spurling RA, Bingel WH. *Metall Mater Trans A* 1998;29A:1955.
- [25] Sato YS, Kokawa H, Enomoto M, Jogan S. *Metall Mater Trans A* 1999;30A:2429.
- [26] Sauvage X, Dede A, Cabello Munoz A, Huneau b. *Mater Sci Eng A* 2008;A491:364.
- [27] Kumar N, Mishra RS, Huskamp CS, Sankaran KK. *Mater Sci Eng A* 2011;528:5883.
- [28] Kumar N, Mishra RS, Huskamp CS, Sankaran KK. *Scripta Mater* 2011;64:576.
- [29] Mishra RS. In: Mishra RS, Mahoney MW, editors. *Friction stir welding and processing*. Materials Park (OH): ASM International; 2007. p. 309.
- [30] Seidman DN. *Annu Rev Mater Res* 2007;37:127.
- [31] Kelly TF, Miller MK. *Rev Sci Instrum* 2007;78:031101.
- [32] Parratt LG. *Probability and experimental errors in science*. New York: Wiley; 1966.
- [33] Marquis EA, Seidman DN, Asta M, Woodward C. *Acta Mater* 2006;54:119.
- [34] Muller EW, Bahadur K. *Phys Rev* 1956;102:624.
- [35] Panitz JA. *Rev Sci Instrum* 1973;44:1034.
- [36] Gault B, Geuser F, Stephenson LT, Moody MP, Muddle BC, Ringer SP. *Microsc Microanal* 2008;14:296.
- [37] Bellon P, Averbach RS, Odunuga S, Li Y, Krasnochtchekov P. *Phys Rev Lett* 2007;99:110602.
- [38] Hellman OC, Vandenbroucke JA, Rusing J, Isheim D, Seidman DN. *Microsc Microanal* 2000;6:437.
- [39] Jo HH, Fujikawa SI. *Mater Sci Eng* 1993;A171:151.
- [40] Kumar N, Mishra RS. Unpublished data.
- [41] Dinsdale K, Harris SJ, Noble B. In: Sanders TH, Starke EA, editors. *TMS proceedings*. Warrendale (PA): TMS; 1981. p. 10–1.
- [42] Hertzberg RW. *Deformation and fracture mechanics of engineering materials*. 3rd ed. New York: Wiley; 1989.
- [43] Frost HJ, Ashby MF. *Deformation mechanism maps*. Oxford: Pergamon; 1982.
- [44] Kendig KL, Miracle DB. *Acta Mater* 2002;50:4165.
- [45] Booth-Morrison C, Dunand DC, Seidman DN. *Acta Mater* 2011;59:7029.
- [46] Meyers M, Chawla K. *Mechanical metallurgy: principles and applications*. Englewood Cliffs (NJ): Prentice Hall; 1984.
- [47] Fu C. *J Mater Res* 1990;5:971.
- [48] George E, Pope D, Fu C, Schneibel J. *ISIJ Int* 1991;31:1063.
- [49] Fukunaga K, Shouji T, Miura Y. *Mater Sci Eng* 1997;A239:202.
- [50] Ardell AJ. *Metall Mater Trans A* 1985;16A:2131.
- [51] JCPDS-International Centre for Diffraction Data, v. 2.00; 1998.
- [52] Hyland R, Stiffler R. *Scripta Metall Mater* 1991;25:473.
- [53] Nembach E. *Particle strengthening of metals and alloys*. New York: Wiley; 1997.
- [54] Ashby MF. In: Kelly A, Nicholson RB, editors. *Strengthening methods in crystal*. Amsterdam: Elsevier; 1971. p. 137.
- [55] Rhodes CG, Mahoney MW, Bingel WH, Spurling RA, Bampton CC. *Scripta Mater* 1997;36:69.
- [56] Liu G, Murr LE, Niou CS, McClure JC, Vega FR. *Scripta Mater* 1997;37:355.
- [57] Sato YS, Park SHC, Kokawa H. *Metall Mater Trans A* 2001;32:3023.
- [58] Krug ME. PhD thesis, Northwestern University, USA; 2011.
- [59] Tabor D. *The hardness of metals*. New York: Oxford University Press; 1951.
- [60] Krug ME, Dunand DC, Seidman DN. *Acta Mater* 2011;59:1700.
- [61] Mahoney M, Mishra RS, Nelson T, Flintoff J, Islamgaliev R, Hovansky Y. In: Jata KV, Mahoney MW, Mishra RS, Semiatin SL, Filed DP, editors. *TMS proceedings*. Materials Park (OH): TMS; 2001. p. 183.
- [62] Zhao J, Jiang F, Jian H, Wen K, Jiang L, Chen X. *Mater Des* 2010;31:306.
- [63] Fuller CB, Seidman DN. *Acta Mater* 2005;53:5415.
- [64] Fuller CB, Krause AR, Dunand DC, Seidman DN. *Mater Sci Eng A* 2002;A338:8.
- [65] Kolli RP, Seidman DN. *Microsc Microanal* 2007;13:272.